Journal of Volcanology and Geothermal Research 260 (2013) 117–126

Contents lists available at SciVerse ScienceDirect

Journal of Volcanology and Geothermal Research

journal homepage: www.elsevier.com/locate/jvolgeores

Tracking the permeable porous network during strain-dependent magmatic flow

J.E. Kendrick [a,b,*], Y. Lavallée [a,b], K.-U. Hess [a], M.J. Heap [c], H.E. Gaunt [d], P.G. Meredith [d], D.B. Dingwell [a]

[a] Department of Earth and Environmental Sciences, Ludwig-Maximilians-Universität, Theresienstr. 41, 80333 Munich, Germany
[b] Department of Earth, Ocean and Ecological Sciences, School of Environmental Sciences, University of Liverpool, Liverpool L69 3BX, United Kingdom
[c] Laboratoire de Déformation des Roches, Équipe de Géophysique Expérimentale, Institut de Physique de Globe de Strasbourg (UMR 7516 CNRS, Université de Strasbourg/EOST), 5 rue René Descartes, 67084 Strasbourg cedex, France
[d] Rock & Ice Physics Laboratory, Department of Earth Sciences, University College London, Gower Street, London, United Kingdom

ARTICLE INFO

Article history:
Received 13 November 2012
Accepted 23 May 2013
Available online 28 May 2013

Keywords:
Magma
Deformation
Rheology
Viscosity
Strain localization
Damage

ABSTRACT

Rheological variations have been postulated as the cause of transitions from effusive to explosive volcanic eruption style. Rheology is integrally linked to the composition and textural state (porosity, crystallinity) of magma as well as the stress, temperature and strain rate operative during flow. This study characterises the rheological behaviour and, importantly, the evolution of physical properties of two magmas (with different crystallinity and porosity) from Volcán de Colima (Mexico) — a volcanic system known for its rapid fluctuations in eruption style.

Magma samples deformed in a uniaxial press at a constant stress of 2.8, 12 or 24 MPa, a constant temperature of 940–945 °C (comparable to upper conduit or lava dome conditions) to strains of 20 or 30% displayed different mechanical behaviour and significant differences in measured strain rates (10^{-2}–10^{-5} s^{-1}). The evolution of porosity, permeability, dynamic Young's modulus and dynamic Poisson's ratio illustrate a complex evolution of the samples manifested as strain-hardening, visco-elastic, constant-rate and strain-weakening deformation. Both magmas behave as shear-thinning non-Newtonian liquids and viscosity decreases as a function of strain. We find that strain localisation during deformation leads to the rearrangement and closure of void space (a combination of pores and cracks) followed by preferentially aligned fracturing (in the direction of the maximum principal stress) to form damage zones as well as densification of other areas. In a dome setting, highly viscous, low permeability magmas carry the potential to block volcanic conduits with a magma plug, resulting in the build-up of pressures in the conduit. Above a certain threshold of strain (dependent upon stress/strain rate), the initiation, propagation and coalescence of fractures leads to mechanical degradation of the magma samples, which then supersedes magmatic flow and crystal rearrangement as the dominant form of deformation. This results in lower apparent viscosities than those anticipated for magma of such crystallinity, especially at high strain rates. In a lava dome, this could result in dome collapse and the concomitant depressurisation could trigger an explosive eruption.

1. Introduction

1.1. Motivation

The frequent and as yet unpredictable transition from effusive to explosive volcanic behaviour is common to active composite volcanoes, yet our understanding of the processes which control this evolution is poor. The rheology of magma, dictated by its composition, porosity and crystal content, is integral to eruption behaviour (McBirney and Murase, 1984; Lejeune and Richet, 1995; Petford, 2003; Caricchi et al., 2007; Lavallée et al., 2007; Cordonnier et al., 2009). Indeed, rheological variations have previously been cited as the cause of effusive–explosive transitions on multiple timescales (Dingwell, 1996; D'Oriano et al., 2005; Lavallée et al., 2008; Cordonnier et al., 2009; Divoux et al., 2011). Fragmentation and explosive eruptions result from the brittle failure of magma at high temperature (Lavallée et al., 2008; Tuffen et al., 2008; Smith et al., 2011) and for a given material, the transition into the brittle regime is initiated by a decrease in temperature or increase in shear stress or strain rate (Dingwell and Webb, 1989; Webb and Dingwell, 1990; Lavallée et al., 2007).

Laboratory experiments which aim to simulate realistic volcanic conditions permit the controlled study of volcanic processes (Pallister et al., 1992; Kennedy et al., 2005; Smith et al., 2009; Hess et al., 2007;

* Corresponding author at: Department of Earth and Environmental Sciences, Ludwig-Maximilians-Universität, Theresienstr. 41, 80333 Munich, Germany.
E-mail address: jackie.kendrick@liverpool.ac.uk (J.E. Kendrick).

0377-0273 © 2013 The Authors. Published by Elsevier B.V. Open access under CC BY-NC-ND license.
http://dx.doi.org/10.1016/j.jvolgeores.2013.05.012

Lavallée et al., 2008; Tuffen et al., 2008; Cordonnier et al., 2009; Heap et al., 2009; Heap et al., 2011; Smith et al., 2011) and aid the development of models to describe the behaviour of magmas in conduit and dome settings (Melnik and Sparks, 1999; Melnik, 2001; Caricchi et al., 2007; Lavallée et al., 2007; Costa et al., 2009; Deubelbeiss et al., 2011). Experiments on magma show that the addition of crystals to a melt increases viscosity at low strain rates. At low crystallinity (<40%), this non-linear increase has been described by the Einstein–Roscoe equation (Roscoe, 1952), as parameterised by Marsh (1981). Above a threshold of crystallinity (defined by the maximum packing fraction, which in itself is dependent upon the size, shape and distribution of the suspended crystals; Cimarelli et al., 2011; Picard et al., 2011) particle–particle interaction permits the transmission of stress via the solid fraction (Petford, 2003) resulting in non-Newtonian rheological behaviour (Lejeune and Richet, 1995; Carreau et al., 1999; Caricchi et al., 2007; Lavallée et al., 2007; Cordonnier et al., 2009; Deubelbeiss et al., 2011). Lavallée et al. (2007) present a rheological law for this non-Newtonian behaviour based on experiments on a wide range of natural magmas which contain a fully connected crystal structure.

In this study we track the damage evolution in experimentally deformed natural magmas for the first time. A magma's ability to degas through the permeable porous network and its propensity for fragmentation are integrally linked to the physical state of the magma, which must be better understood to predict volcanic behaviour. The samples chosen are from Volcán de Colima (Mexico), a volcano which experiences regular transitions in eruption style. The initial rock-physical, chemical and microstructural properties of the samples were characterised using porosity and permeability measurements, ultrasonic wave velocity measurements (that were also used to determine dynamic Young's modulus and Poisson's ratio), X-ray fluorescence, scanning electron and optical microscopy, X-ray computed tomography and differential scanning calorimetry. Then, following episodes of high-temperature deformation (at different stresses), the evolution of the physical properties and the microstructural state of the samples were tracked by systematically re-measuring porosity, permeability, ultrasonic wave velocities, and by re-imaging the samples through X-ray computed tomography.

1.2. Volcán de Colima, history and erupted products

Volcán de Colima is an active volcano which, together with the extinct Nevado de Colima, forms the Colima Volcanic Complex, located in the Trans-Mexican Volcanic Belt. The current eruptive period is part of an ~100-year cycle of explosive to effusive events which culminate in Plinian eruptions (Luhr and Carmichael, 1980; Breton et al., 2002; Luhr, 2002). The current period of activity was marked at its onset by an increase in volcano-tectonic (VT) seismicity which began in November 1997 (Dominguez et al., 2001; Navarro-Ochoa et al., 2002; Zobin et al., 2002), and which was swiftly followed by a dome-building episode and multiple lava flows (in November 1998). This transitioned into periodic explosive behaviour in 1999 and early 2001, and formed a summit crater. Subsequently, effusive behaviour recommenced forming a lava dome, which eventually overflowed the crater in February 2002 and flowed down the northern flanks (Varley et al., 2010). In March 2003 the eruption once again transitioned to explosive behaviour, whereby repeated Vulcanian explosions occurred over 18 months. These subsided as a new phase of block-lava extrusion occurred during late 2004 (Zobin et al., 2008), but resumed in December 2004. During May and June 2005, following numerous swarms of long period (LP) events which indicated ascending magma (Varley et al., 2010; Arámbula-Mendoza et al., 2011), a number of dome-building eruptions and larger Vulcanian events occurred, with associated column collapses and pyroclastic flows (Gavilanes-Ruiz et al., 2009). A new dome began to form in early 2007, and in early 2010 the dome was growing by approximately 2000 m^3/day (James and Varley, 2012) before eventually

Fig. 1. Lava dome. Arial photograph of the lava dome at Volcán de Colima, pictured here in November 2012.

overflowing the crater rim (Lavallée et al., 2012). During late 2010 multiple incandescent landslides travelled down the North, South and Western flanks of the volcano. In January 2011 "dust plumes" from landslides were sighted over the 2.6 million m^3 lava dome (Fig. 1), which stopped growing between June 2011- December 2012, but has since reawakened.

Despite the frequent fluctuations in eruptive style at Volcán de Colima, there is little variation in the erupted products, which tend to be highly crystalline, intermediate, andesitic lavas (Mora et al., 2002; Valdez-Moreno et al., 2006). Lavallée et al. (2012) found that recent dome lavas contain approximately 30 vol.% phenocrysts, 25–50 vol.% microlites and 14–45 vol.% glass. Porosity is highly variable between 1 and 30% (Kolzenburg et al., 2012; Lavallée et al., 2012), with a bimodal distribution showing peaks at 12 and 26%. Plagioclase, diopside and hypersthene dominate the crystal assemblage, forming a porphyritic texture. Hornblende phenocrysts occur sporadically and olivine and iron-titanium oxides occur as xenocrysts, all of which reside in a peraluminous, rhyolitic interstitial glass. Exceptions are the more mafic (Luhr and Carmichael, 1990; Luhr, 2002; Savov et al., 2008) culminating explosive eruptions of the 100-year cycles (González et al., 2002), which are attributed to the influx of mafic magma into the magma chamber from a deeper reservoir. Magma is largely degassed by the time it reaches the surface (Reubi et al., 2013), and Atlas et al. (2006) suggest vapour-saturated crystallisation during ascent at depths of less than 12 km. Melt inclusions measure H_2O concentrations of 0.1 to 2.5 wt.% and CO_2 concentrations of up to 800 ppm (Reubi et al., 2013), indicating trapping conditions of 10–150 MPa and 959–1015 °C. Correspondingly, Savov et al. (2008) suggest storage temperatures of 960–1020 °C based on geothermometry of pyroxenes.

2. Method

2.1. Sample selection

The two sample materials chosen for this study are the andesites COL-B2 and COL-LAH4 (Table 1, Fig. 2A and E) from the dome-building eruptions and explosions that occurred during 2004. The two sample materials were selected on the basis of their contrasting initial porosities and crystal contents. The two lavas contain 9.5 and 27.2% porosity (a combination of cracks and pores), 34 and 20% phenocrysts, 31 and 23% microlites, and 26 and 30% interstitial melt for B2 and LAH4, respectively. The andesites from this particular eruptive period are isotropic, evidenced both seismically (by use of ultrasonic wave velocity measurements) and optically (by thin section and tomographic

Table 1
Geochemical composition of bulk rock and interstitial glass for both samples normalised to 100%. Where $_t$ = total. Loss on ignition of 0.32 and 0.00 for B2 and LAH4 respectively.

Sample	SiO_2	Al_2O_3	FeO_t	MnO	MgO	CaO	Na_2O	K_2O	TiO_2	P_2O_5	L.O.I.	Total
B2 bulk[a]	60.89	17.93	5.72	0.10	2.82	5.81	4.76	1.34	0.60	0.20	0.32	100.49
B2 glass[b]	72.48	13.21	2.86	0.05	0.24	1.69	5.03	2.90	0.67	0.08	–	99.21
LAH4 bulk[a]	59.10	17.45	6.13	0.11	4.04	6.62	4.52	1.19	0.62	0.19	0.00	99.97
LAH4 glass[b]	74.26	12.89	2.14	0.04	0.44	1.81	4.45	3.05	0.59	0.31	–	99.98

[a] Measured by X-ray fluorescence.
[b] Measured by wavelength dispersive analysis in a CAMECA SX100 scanning electron microprobe.

imaging). The glass transition temperatures (T_g) of the interstitial glasses, established by differential scanning calorimetry (DSC) at a heating/cooling rate of 10 °C/min (on approx. 25 mg glass chips) are 746 ± 3 °C for B2 and 751 ± 3 °C for LAH4. Rheological measurements are used to track the non-Newtonian viscosity using experiments at realistic volcanic conditions and for comparison with complementary microstructural data.

2.2. Viscosity press

A high-temperature uniaxial press (Fig. 3) was used to study the rheological evolution of crystalline andesite from Volcán de Colima under different applied stresses (see Hess et al., 2007 for experimental setup and procedure). Cylindrical samples 50 mm in length with 25 mm diameter (aspect ratio of 2:1, as per the guidelines of Hawkins,

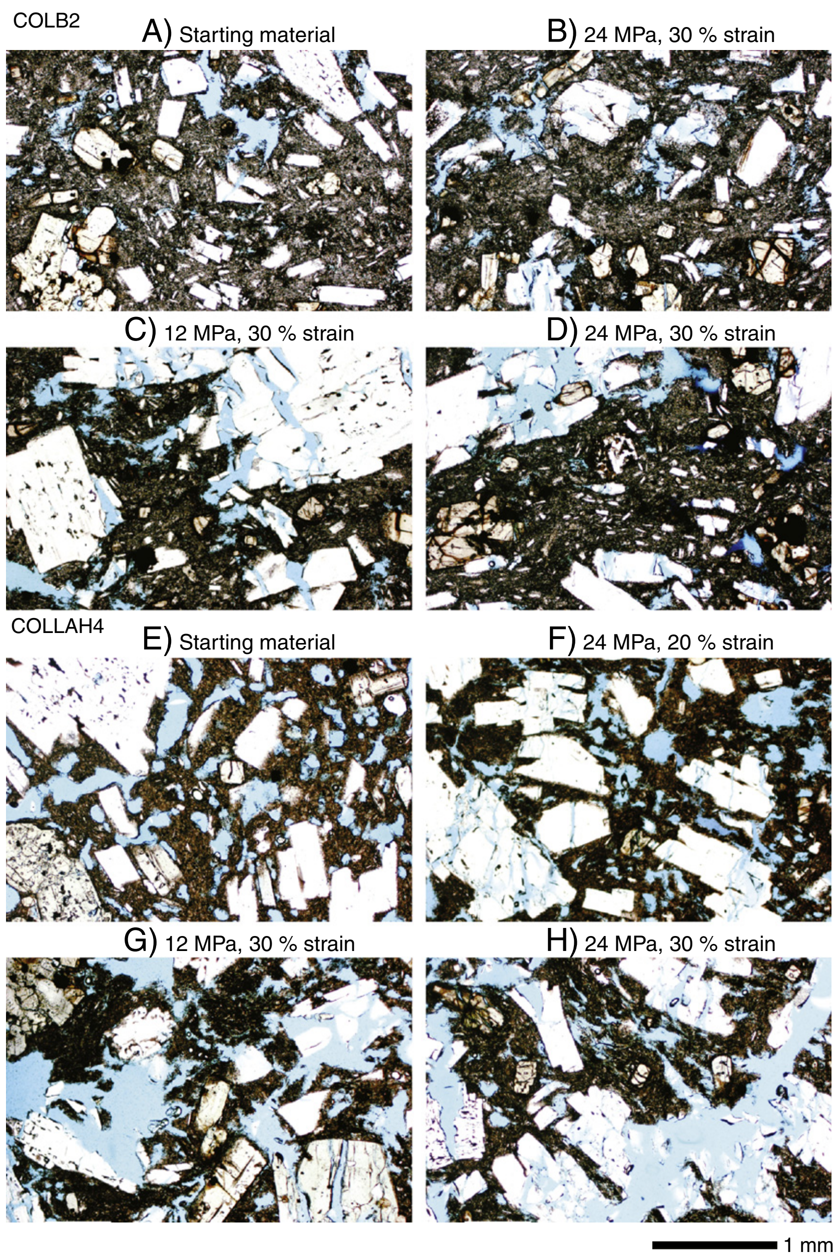

Fig. 2. Damage evolution. Photomicrographs to show the appearance of Colima samples B2 (A–D) and LAH4 (E–H), and the evolution of phenocrysts, microlites, interstitial glass and pores/cracks after deformation.

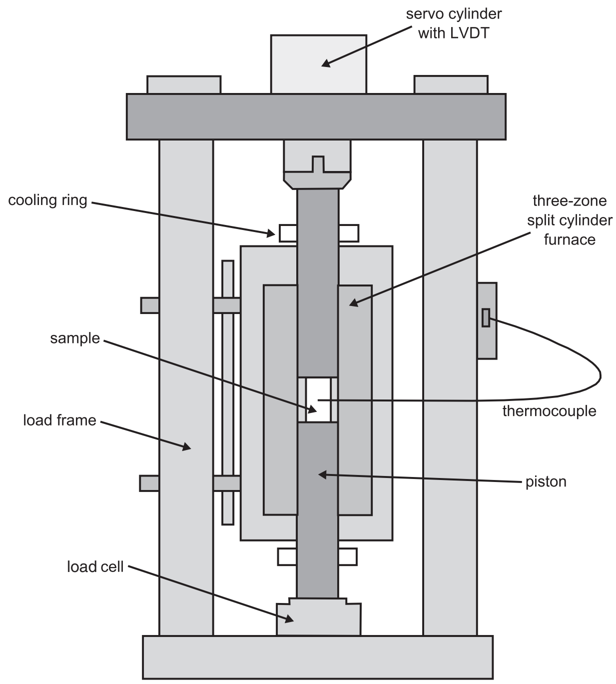

Fig. 3. Deformation apparatus. Schematic diagram of the high-temperature uniaxial press used for the deformation experiments and viscosity measurements at Ludwig-Maximilians-Universität, Munich.

1998) were heated at a furnace heating rate of 2 °C/min until the sample was at a steady 940–945 °C (measured using a thermocouple in the centre of the sample). This heating rate allows ample time for equilibration of the system in order to minimise the effect of thermal gradients (see Yong and Wang, 1980). The desired stresses of 2.8, 12 or 24 MPa were applied instantaneously and displacement measured at a rate of 10 measurements/s to 10 or 15 mm axial displacement (20 and 30% strain). After deformation the samples' microstructural state was re-imaged using X-ray computed tomography. They were then cored back into cylinders of 25 mm (removing the lateral bulge) before measuring their rock-physical properties. Finally, once all of the measurements were complete, the samples were thin sectioned for optical microscopy.

One of the goals of this study was to monitor the evolution of rock-physical properties and microstructural state as a function of high-temperature deformation. While we do not anticipate that “magma” and “rock” properties will be identical, our interest lies in monitoring changes in their physical and microstructural properties (whether porosity increases or decreases, for example, after deformation). The frozen-in “rock” properties are a representation of the properties of the “magma” as it is not yet possible to measure porosity and permeability during deformation at 940–945 °C.

2.3. Microstructural characterisation

Thin sections and tomographic images were made from both the starting materials and the deformed cores. 3D high-resolution tomography images were acquired through v|tome|x s240 micro-CT scanner from GE phoenix using a high-power X-ray tube and a drx-250 rt detector system (experimental conditions: pixel/voxel size: 30.0 μm, 1000 images for 360° (average of 3 single images, one image skipped), exposure time of 1 s, voltage of 80 kV and current of 250 μA).

2.4. Physical property characterisation

Connected water porosity was measured via the Archimedes buoyancy method (Guéguen and Palciauskas, 1994). Water (distilled) permeability was measured in a servo-controlled steady-state-flow permeameter in the Rock & Ice Physics Laboratory at University College London (see also Kolzenburg et al., 2012) under effective pressures of 5–50 MPa (Fig. 4). For the purpose of this study we assume that the effective pressure is simply the confining pressure minus the pore fluid pressure (i.e. we assume that the poro-elastic constant α is equal to one, see Guéguen and Palciauskas, 1994). The “upstream” (P_{up}) and “downstream” (P_{down}) pore fluid pressures were 9.5 MPa and 10.5 MPa, respectively (i.e., there was a 1 MPa pressure differential across the sample). Once steady-state flow had been established, water permeability (κ_{water}) was calculated using Darcy's law:

$$Q/A = \kappa_{water}/\eta L\left(P_{up} - P_{down}\right) \quad (1)$$

where Q is the volume of fluid measured per unit time, A is the cross-sectional area of the sample, η is the viscosity of the pore fluid, and L is the length of the sample.

Bench-top ultrasonic wave velocity measurements, i.e. P- (V_p) and S-waves (V_s), were made on nominally-dry samples (vacuum dried at 40 °C for at least 24 h) at the Laboratoire de Déformation des Roches (Strasbourg) and used to calculate dynamic Young's modulus (Eq. (2)) and dynamic Poisson's ratio (Eq. (3)):

$$E_d = \rho V_s^2\left(3V_p^2 - 4V_s^2\right)/\left(V_p^2 - V_s^2\right) \quad (2)$$

$$\nu_d = \left(V_p^2 - 2V_s^2\right)/\left(2V_p^2 - 2V_s^2\right) \quad (3)$$

where E_d is Young's modulus, ρ is the bulk sample density and ν_d is Poisson's ratio. We note that the flow direction for our permeability measurements and the propagation direction for our elastic wave measurements are parallel to the maximum principal stress (i.e. the direction of loading) in our deformation experiments. The dynamic Young's modulus and Poisson's ratio calculated in this study differ from those calculated using the stress–strain response of a sample under a constant strain rate (i.e., static elastic moduli) due to their frequency-dependence (see Heap et al., 2010; Kendrick et al., 2013 and references therein).

3. Results

3.1. Magma rheology

The two magmas deform differently at any given temperature and applied stress, with resultant strain rates varying between 10^{-2} and 10^{-5} s^{-1} (Fig. 5A). Strain rates are always higher at higher stress, and

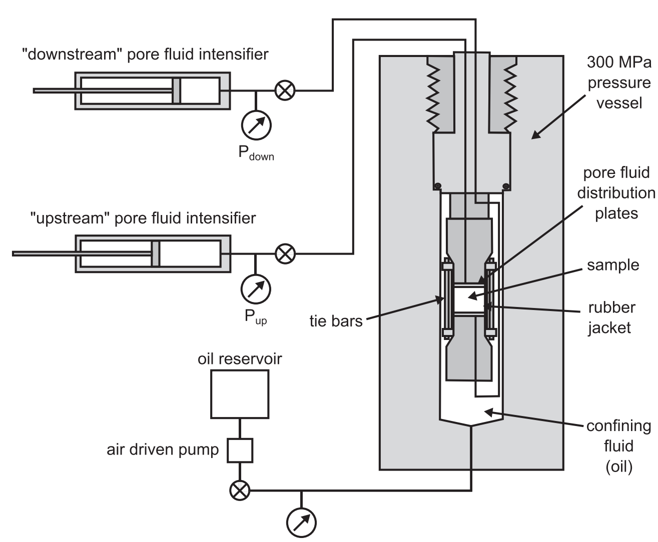

Fig. 4. Permeameter. Schematic diagram of the permeameter at University College London.

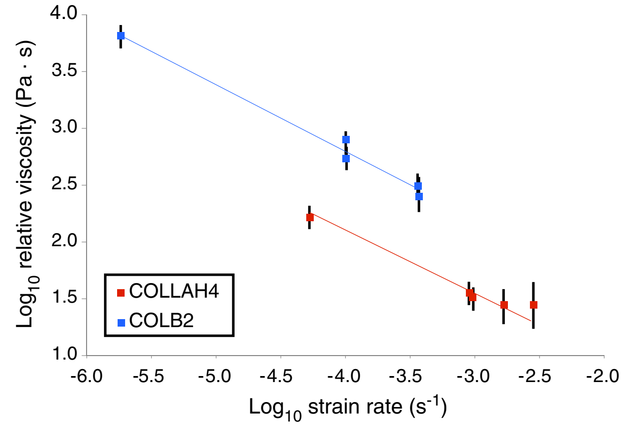

Fig. 6. Viscosity variation with strain rate. The change in relative viscosity with strain rate depicts a linear negative trend for both samples under the investigated range, evidence of the shear-thinning behaviour of magma.

higher for LAH4 (10^{-2} to 10^{-4} s^{-1}) than for B2 (10^{-3} to 10^{-5} s^{-1}) under the same applied stress. Thus LAH4 is either weaker or less viscous. A difference in the evolution of strain rate with increasing total strain presents an interesting contrast between samples. All of the magma deformation experiments show initial reduction in strain rate with increasing strain, as a result of strain-hardening (Fig. 5). Under just 2.8 MPa of stress, both samples continue to exhibit strain-hardening until at least 20% strain, though the effect lessens as total strain increases and the total effect is larger for B2 (Fig. 5A). For B2, strain hardening transitions to constant strain rate deformation at ~5% and ~3% strain at 12 and 24 MPa, respectively, and continues to a total strain of up to 30%. For LAH4, strain hardening ends at 1–2% strain and deformation proceeds at a constant strain rate, however, at 24 MPa this further transitions into strain-weakening behaviour at ~25% strain (Fig. 5A). This is an indication that B2 and LAH4 have significantly different mechanical properties, which, given the similarity in composition and T_g, must relate to the structural attributes of the samples, including crystal content, crystal size distribution and porosity (including pore size/shape distribution and pore versus crack porosity).

The apparent viscosity (η_a) of the samples during flow was calculated using Eq. (4) from Gent (1960), where F is the force (in N), h is the change in length during the experiment (in m), V is the initial volume of the sample (in m^3) and t is time (in s):

$$\eta_a = 2\pi F h^5 / 3V\left((dh/dt)2\pi h^3 + V\right). \tag{4}$$

Under the same applied stress, apparent viscosity was higher in B2 (10^{10} to 10^{11} Pa·s) than in LAH4 (10^{9} to 10^{10} Pa·s) (Fig. 5B). For both samples the viscosity was lower at higher applied stress, demonstrating dominantly pseudo-plastic (shear-thinning) material characteristics (Caricchi et al., 2007; Cordonnier et al., 2009; Lavallée et al., 2012). Both B2 and LAH4 exhibit strain-hardening behaviour to at least 20% strain at just 2.8 MPa (Fig. 5B). At 12 and 24 MPa this does not occur in LAH4 and persists to less than 5% strain in B2, after which viscosity decreases over time (and strain, Fig. 5B), a phenomenon termed “time-dependent” deformation (Cordonnier et al., 2009). For sample

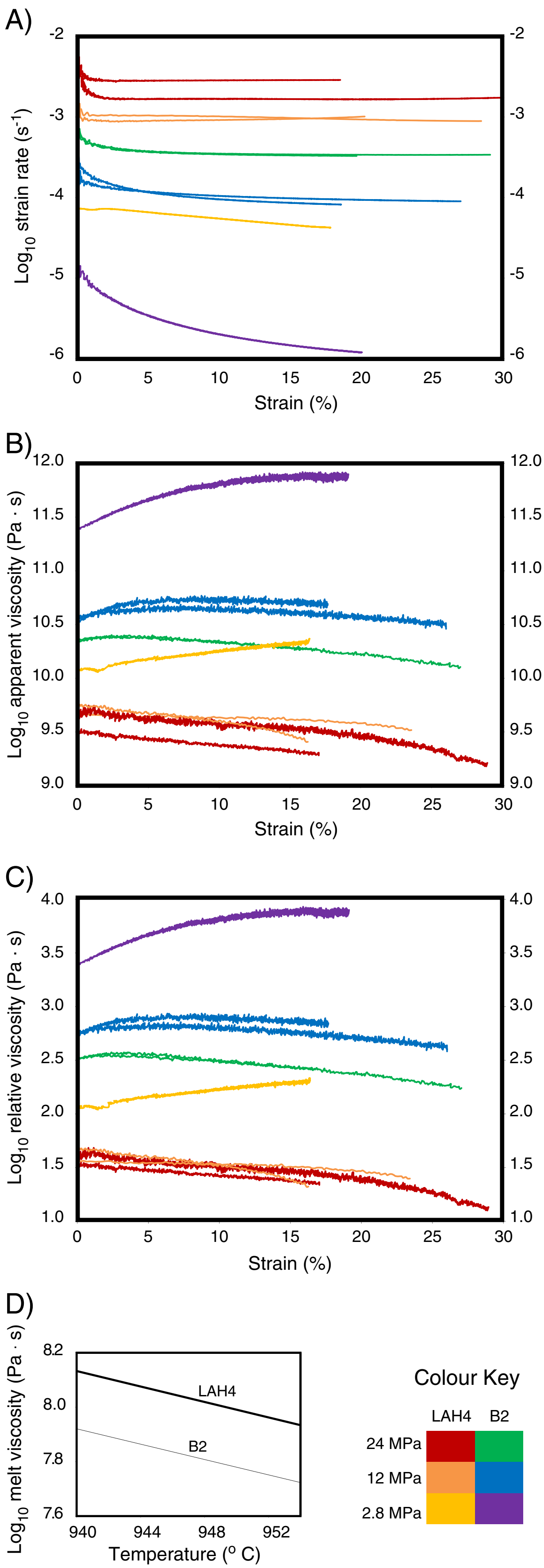

Fig. 5. Rheological development. A) The evolution of strain rate with total strain for samples B2 and LAH4 under 2.8, 12 and 24 MPa stress. B) Rheological behaviour of samples B2 and LAH4 under 2.8, 12 and 24 MPa stress, showing the changing apparent viscosity as a function of total strain. C) “Strain-dependent” deformation; relative viscosity as a function of strain, with the effect of temperature excluded shows concomitant deformation rate independent of stress and crystallinity. D) Interstitial melt viscosities over the experimental temperature range as calculated from the GRD viscosity model (Giordano et al., 2008) using glass chemical composition established by WDA.

Table 2
Timescale of experiments.

Sample	Stress (MPa)	Strain (%)	Time (s)
B2	28.4	19.7	600
	28.4	29.1	858
	15.9	18.6	2276
	15.8	27.1	3010
	2.8	20.0	167,850
LAH4	28.4	18.6	64
	26.4	30.1	173
	15.3	20.3	200
	15.9	28.5	320
	2.8	17.8	4228

LAH4 at 24 MPa there is an acceleration in the rate of viscosity decrease after 25% strain, concordant to the slight increase in strain rate (Fig. 5A).

The non-Newtonian character of the melt is further investigated by plotting the relative viscosity against strain (Fig. 5C), which isolates the effect of crystal content from the temperature dependence (Lejeune and Richet, 1995), which may result in part from viscous heating. The relative viscosity (η_r) relates the apparent viscosity (η_{app}) of the sample to the viscosity of the melt (η_{melt}) at the monitored experimental temperature in Eq. (5):

$$\eta_r = \eta_{app}/\eta_{melt} \quad (5)$$

where η_{melt} was calculated for the experimental temperature range using the GRD viscosity model (Giordano et al., 2008) from chemical composition of the interstitial melt (measured by WDA, Table 1). We find that the relative viscosity is always higher for B2 than LAH4 (Fig. 6), due to the higher apparent viscosity (Fig. 5B) and lower interstitial melt viscosity of B2 (Fig. 5D). The strain-hardening behaviour of the low-stress experiments (2.8 MPa) and the shear-thinning effect of the higher-stress experiments (12–24 MPa), reveal similar trends for both samples when plotted against strain (it is not dependent upon crystal content within the ranges measured, Fig. 5C), indicating that, as different applied stresses resulted in such different timescales of experiments (Table 2) the degradation, deformation and structural reorganisation of magma (shown in Figs. 1 and 7) may be strain, rather than time, dependent.

In order to verify our findings, the data from Lavallée et al. (2012) were incorporated with those from this study in Fig. 8. We find that the resultant strain rate for samples B2 and LAH4 under a given applied stress at known temperature is in accordance with previous data (within the errors stated in Lavallée et al., 2012). It thus follows that the non-Newtonian exponent of 0.5, and the rheological relationship between strain (σ), strain rate (γ) and temperature above the glass transition ($T - T_g$), stated by Lavallée et al. (2012) in Eq. (6) are therefore likely to be applicable to these magmas:

$$\text{Log}\sigma = 0.5\,\text{Log}\gamma + 606.9/T - T_g + 0.29. \quad (6)$$

The data for sample LAH4 falls slightly below and B2 falls slightly above the predicted viscosities (within the error stated in Lavallée et al., 2007), a difference surely caused by the different structural properties of the samples (as clearly evidenced in Figs. 2 and 7), which may have a larger impact than previously acknowledged.

3.2. Physical properties

The evolution of connected porosity, dynamic Young's modulus, dynamic Poisson's ratio (Fig. 9) and water permeability (Fig. 10) with increasing deformation quantifies the damage induced by high-temperature uniaxial compression depicted in the tomography images (Fig. 7). For B2 high-temperature uniaxial deformation leads to an increase in porosity, whereas for LAH4 porosity is decreased under 12 MPa to 20% strain. The 12 MPa and 20% strain experiments did not change permeability (although the sample of LAH4 lost its cohesion at an effective pressure of 20 MPa during the permeability measurements,

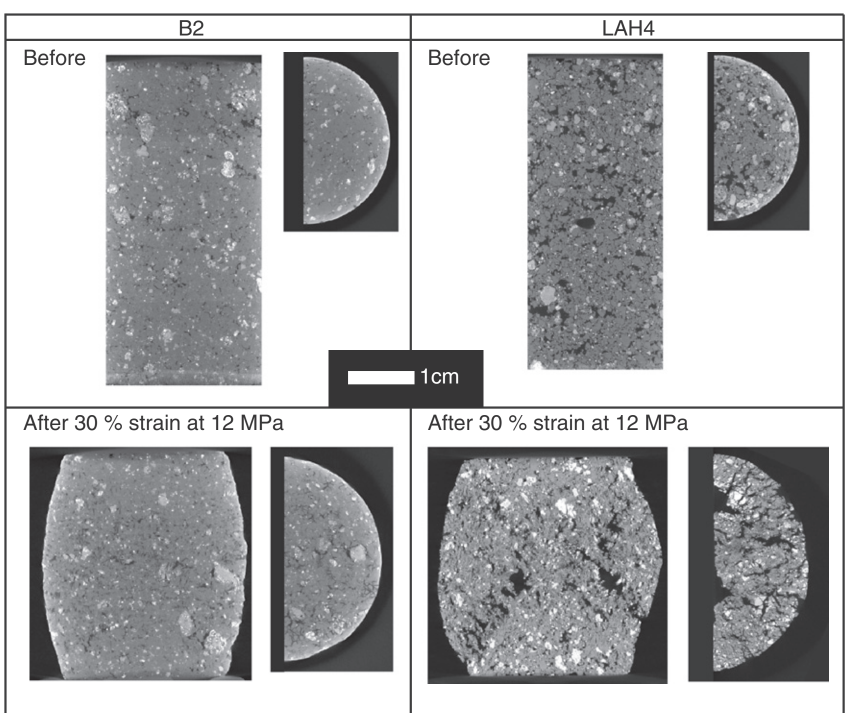

Fig. 7. 3D reorganisation due to deformation. X-ray computed tomography images of starting materials and cores deformed to 30% strain at 12 MPa. Images show a vertical and horizontal cross section and are to scale, highlighting the shortening and extensive lateral expansion of the deformed samples. The reorganisation of pore space is clear in both samples, and in LAH4 2 clear damage zones are seen running diagonally through the sample.

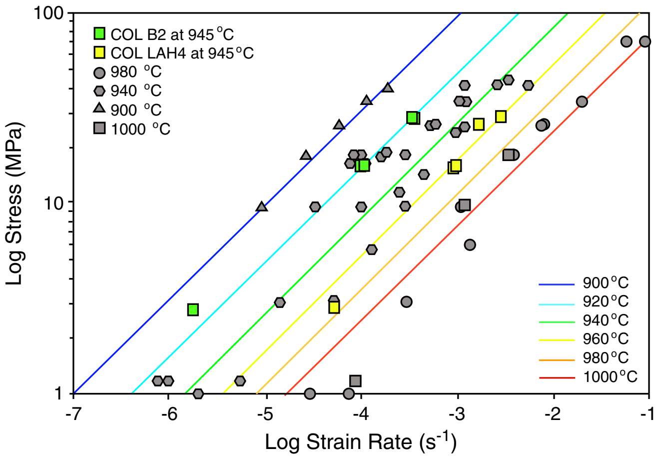

Fig. 8. Shear-thinning behaviour of magma. Shear-thinning effect evidenced by the linear relationship of Log stress versus Log strain rate established by (and including data in grey from) Lavallée et al. (2012). Sample LAH4 has a lower viscosity than expected and B2 has a slightly higher viscosity, highlighting the importance of understanding the physical magma and rock properties.

Fig. 10), and Poisson's ratio decreased and Young's modulus increased (Fig. 9), indicating a stiffening of the material in the axial direction.

By increasing strain to 30% at 12 MPa, the Poisson's ratio increases and Young's modulus decreases, such that both values become comparable to the starting material (Fig. 9). At 30% strain, the permeability of the material is reduced for sample B2 (Fig. 10). However, the sample of

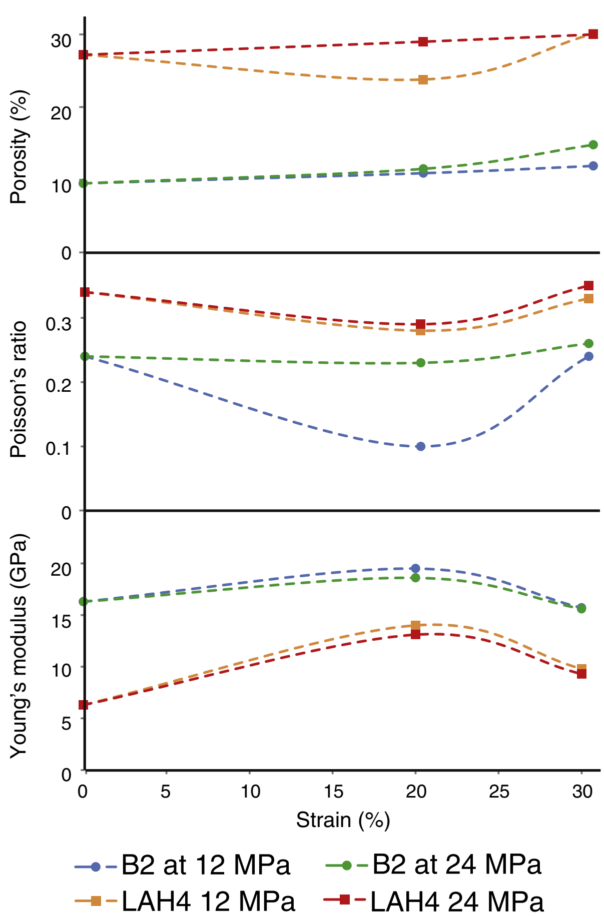

Fig. 9. Physical properties of the samples. The evolution of porosity, Poisson's ratio and Young's modulus from the starting material to deformed products, points represent measured values and dashed lines infer the evolution.

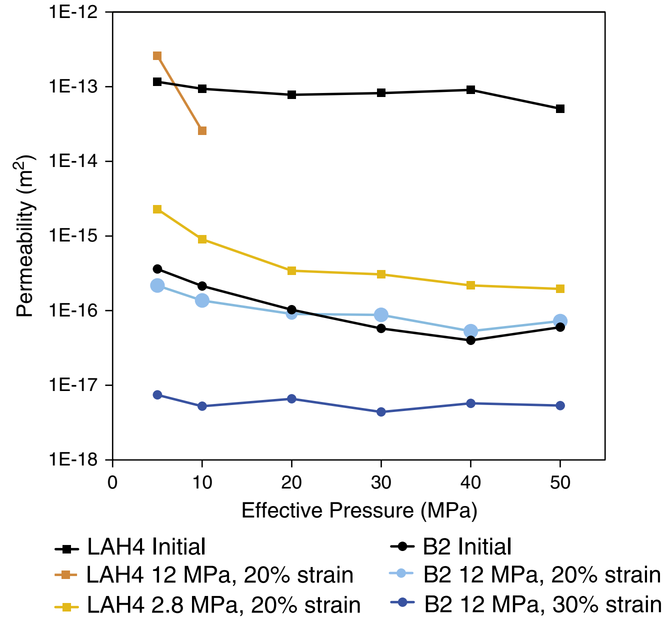

Fig. 10. Permeability evolution. Steady-state water permeability measured at effective pressures of 5–50 MPa for samples B2 and LAH4 (natural and deformed at 2.8 or 12 MPa to a total of 20 or 30% strain).

LAH4 deformed to 30% strain was unable to sustain pressure in the permeameter to even 5 MPa effective pressure and ruptured (indicating further weakening compared to the starting material and the sample deformed at 20% strain). The permeability of LAH4 was, however, decreased at the lower stress of 2.8 MPa to 20% strain (Fig. 10).

Upon increasing the stress to 24 MPa and deforming to 20% strain, Poisson's ratio and Young's modulus also indicate a stiffening of both materials, although in this instance the porosity of LAH4 is now also increased, contrary to the results at 12 MPa. By increasing the strain to 30%, the Young's modulus decreases (for B2, to slightly below the starting material, whereas for LAH4, still considerably above) and Poisson's ratio increases (Fig. 9). However, even in the most deformed samples, Poisson's ratio and Young's modulus values are similar to the starting material, but there is a complex evolution of stiffening and softening beforehand. We note that increasing the strain has a larger effect on porosity, Young's modulus and Poisson's ratio than increasing the stress over the investigated ranges, and that the effect of both stress and total strain on permeability evolution is significant, with lower stresses and higher strains reducing permeability the most.

4. Discussion

The progressive rheomechanical behaviour of the magmas is complex, but can be summarised as follows:

1) An initial recoverable elastic strain during which no fracturing occurs.
2) Above 1% strain the behaviour of the samples deviates: both sample sets deformed at 2.8 MPa proceed with strain-hardening behaviour to at least 20% strain, corresponding to a decrease in permeability. At 12 or 24 MPa samples of B2 have a strain hardening portion at the onset of loading (to ~5% strain). In contrast, despite the sudden drop in strain rate early in the loading, samples of LAH4 does not exhibit strain-hardening at either 12 or 24 MPa (Fig. 5).
3) For the experiments at 12 or 24 MPa, constant strain rate is achieved after the elastic strain portion for LAH4 and after the strain-hardening for B2 (Fig. 5A). This stage initiates marginally sooner (lower strain) at higher stresses (and thus strain rate). For both samples the behaviour is shear-thinning (Fig. 6). Under a

uniaxial stress of 12 MPa, both samples achieve 30% strain without evidence of an approach to brittle failure, although fractures are seen to coalesce in LAH4 (Fig. 7). Here, permeability remains unchanged at 12 MPa and 20% strain, but structurally degrades LAH4 (evidenced by sample rupture during permeability measurements). As strain increases, permeability is reduced for B2, but sample LAH4 is weakened despite elastic moduli which indicate stiffening for both samples; hence the strain is primarily controlling the reorganisation of the crystals in multi-phase magma.

4) At 24 MPa there is an acceleration in the rate of apparent and relative viscosity decrease for LAH4, which must result from the structural breakdown of the material after 25% strain. Fractures coalesce and form pervasive damage zones (Figs. 2 and 7). This is not seen in the B2 samples.

The rheological behaviour of B2 is in accordance with the rheological relationship depicted in Lavallée et al. (2012) for magmas with solid-fraction crystal contents of at least 50 vol.% (Fig. 8) but, for LAH4, a lower-than-anticipated viscosity results from a structural reorganisation and weakening of the material. Apparent and relative viscosity vary as a function of applied stress, and thus deformation is strain rate dependent. For both samples the viscosity was lower at higher applied stress, but under the same applied stress, apparent viscosity was higher in B2 than in LAH4 (Fig. 5C). Relative viscosity was also higher in B2 than in LAH4, which attests to the higher apparent viscosity (Fig. 5B) and higher interstitial melt viscosity (Fig. 5D), but is also a result of rapidly increasing damage in LAH4 (Figs. 2 and 7). The fact that LAH4 is both less viscous and weaker must relate to the structural attributes of the samples, including crystal content, size and distribution and porosity (including pore size/shape distribution and pore versus crack porosity). Indeed, the Young's moduli of the starting materials (Fig. 9) verify that LAH4 is less stiff than B2, and the higher Poisson's ratio attests to the higher porosity of LAH4.

Apparent and relative viscosity increased with increasing strain at low stress (2.8 MPa) for both samples, showing strain-hardening behaviour. Additionally the elastic portion at the onset of loading in sample B2 at higher load was strain-hardening. In the higher stress experiments (12–24 MPa) viscosity decayed under constant stress, a phenomenon known as pseudo-plastic behaviour and previously referred to as “time-dependent” deformation (Cordonnier et al., 2009). Over time, this effect was faster at higher stress, and also faster in LAH4 than in B2. However, this difference was negated by comparing diminishing viscosity with strain, for which the rates were comparable for B2 and LAH4 (Fig. 5B). It becomes more apparent still by comparing relative viscosity changes with strain (Fig. 5C), that this “time-dependent” deformation of multi-phase suspensions under constant stress is not dependent upon crystal content (under the ranges investigated) or indeed time and instead, is controlled primarily by total strain. The “strain-dependent” deformation must then result partially from magmatic flow and rearrangement of the suspended crystals (as evidenced by thin section and tomography imaging in Figs. 2 and 7) and partially from deformation of the crystals during the unavoidable crystal–crystal interactions which occur when a maximum packing fraction is exceeded, such that particles are forced to interact and transmit stresses (Petford, 2003). The acceleration in the viscosity decrease exhibited by LAH4 at 24 MPa at strains above ~25% (Fig. 5B and C), marks the onset of bulk sample failure, as fractures reach the stage of growth and coalescence (Figs. 2 and 7).

The evolution of Poisson's ratio and Young's modulus differs between samples, but may be summarised as an initial stiffening of the samples during the strain-hardening period where pre-existing cracks and compliant pores orientated sub-perpendicular to the applied stress are closed. The subsequent period of visco-elastic deformation comprises further sub-perpendicular pore and crack closure and ductile deformation of the glass and groundmass, which increases the Young's modulus and lowers the Poisson's ratio. The competition between the closure of sub-perpendicular cracks and pores, and the opening of parallel (i.e. orientated axially) cracks inside the crystals, results in a net reduction in porosity (which contributes to the shear-thinning nature of the magma). However, permeability remains unchanged in the samples deformed at 12 MPa to 20% strain. We contend that, although the net porosity was reduced, the porosity used for fluid flow (i.e. cracks and pores aligned parallel to the flow direction) will remain open (and new cracks orientated parallel to flow are restricted to phenocrysts and do not connect), thus explaining the unchanged permeability. However, the sample of LAH4 deformed at 12 MPa to 20% strain failed under pressurisation for permeability measurements above at an effective pressure of 20 MPa, an indication of weakening as compared to the starting material.

By further increasing the strain to 30% the Young's modulus in B2 is finally decreased, indicating a reduction in sample stiffness (independent of stress), but the sample deformed at 12 MPa actually has a lower permeability than the starting material. We postulate that this is a result of sample geometry, whereby at the top and bottom of the sample deformed under uniaxial compression there is a densification of the material (see Fig. 7) between the diagonally-aligned shear zones. Despite presumably elevated permeability along the shear zones and in the central portion, the permeability in the axial direction is controlled by the least permeable layer. From thin section analysis we find that fractures initiate in phenocrysts, which are more brittle and hence more readily fractured than the surrounding melt and microlites (Cordonnier et al., 2009). During inevitable crystal–crystal interaction, the fractures tend to propagate along the axis of principal stress (i.e. vertically in the phenocrysts in Fig. 2) to eventually form diagonal damage zones seen in Fig. 7. For LAH4 the sample deformed at 12 MPa to 20% strain failed under an effective pressure of 20 MPa during the permeability measurements, which must have forced coalescence of adjacent fractures seen in Figs. 2 and 7. Rheological data supports the physical observations: constant-rate, shear-thinning deformation persists for B2 until at least 30% strain, however in LAH4 it gives way to the onset of mechanical degradation above ~25% strain. Bulk sample failure ensues, evidenced by a rapid increase in strain rate under constant stress. The sample deformed to 30% was weakened so substantially that it was unable to sustain any pressurisation for permeability measurements, despite the fact that the dynamic elastic moduli indicate stiffening. Alternative measurements made on the sample deformed at 2.8 MPa show a significant decrease in permeability (Fig. 10), a result of on-going strain-hardening behaviour throughout the experiment (Fig. 5B and C), an indication of densification of the material.

The damage accumulation in the originally-isotropic samples is highly anisotropic (pre-existing cracks and compliant pores orientated sub-perpendicular to the applied stress will close, and new cracks will form parallel to the applied stress). As a result, our ultrasonic wave velocities and dynamic elastic moduli (measured in the axial direction) will contain some bias. Therefore, we consider that our values represent a “minimum” in the evolution of elastic properties of deformed magma. We must also note that, since the deformation at a volcano could be considered to evolve quasi-statically, rather than dynamically, it has been suggested that static elastic moduli are more appropriate for the modelling of volcanic hazards (Heap et al., 2009; Kendrick et al., 2013; Manconi et al., 2010).

5. Volcanological significance

Understanding the behaviour of multi-phase magmatic suspensions under realistic volcanic conditions is vital to the development of eruption dynamic models and forecasting volcanic activity. The sequence of processes which control the common fluctuations between effusive and explosive eruption style remain poorly understood, despite the common occurrence at dome-building volcanoes such as Volcán de Colima and Montserrat (Lensky et al., 2008). The results of the experiments reported in this study, in conjunction with analysis of the physical properties measured allow us to examine the transition in deformation style in detail, which will help to improve our rheological models of magma transport and volcanic unrest (Melnik and Sparks, 1999; Melnik, 2001; Caricchi et al., 2007; Lavallée et al., 2007; Lensky et al., 2008; Costa et al., 2009; Deubelbeiss et al., 2011). We find that highly crystalline magmas exhibit significantly higher viscosities when deformed more slowly. An order of magnitude change in stress, manifested as 2 orders of magnitude change in strain rate, changes the viscosity by 1–2 log units, providing evidence of shear-thinning behaviour. Such changes, experienced over the timescale of volcanic unrest, could result in the observed acceleration in deformation prior to an explosive eruption (Sparks, 2003; Lensky et al., 2008). Indeed rheological variations, monitored in our study via an increase in damage by fracturing towards the brittle field, have frequently been cited as the cause of effusive to explosive transitions (Dingwell, 1996; D'Oriano et al., 2005; Lavallée et al., 2008; Cordonnier et al., 2009; Divoux et al., 2011). Deformation of magmas can result in a rearrangement of porosity, from void spaces and fractures distributed evenly throughout the sample, to preferred orientations and coalescence into damage zones. Permeable zones form preferentially where strain is localised (Laumonier et al., 2011), affecting the ability of magma to effectively degas through the permeable porous network. Hence, highly viscous, low permeability magmas carry the potential to block volcanic conduits with a magma plug, resulting in the build-up of pressures in the conduit (e.g., Lensky et al., 2008). Plug formation may lead to repetitive "drumbeat" seismicity (Iverson et al., 2006; Lensky et al., 2008), spine extrusion (Nakada et al., 1999; Sparks and Young, 2002; Vallance et al., 2008) and if disrupted, an eventual explosive eruption. Here, we demonstrate that the apparent viscosity of multi-phase magmas is not only dependent on the melt viscosity and crystal and pore contents, but is also dependent upon the "strength" of the magma; mechanical degradation of a material can result in lower apparent viscosities than anticipated, especially at high strain rates, but this is because failure of the sample has already occurred. In a lava dome setting this is manifested as dome collapse (which may not be predicted if the material properties are not understood), which can initiate catastrophic explosive eruptions due to unloading and depressurisation (Melnik and Sparks, 2005; Edmonds and Herd, 2007) and is a significant risk at Volcán de Colima and other stratovolcanoes.

6. Conclusions

This study shows that, at a given temperature and stress, chemically similar lava types can display a significant range of measured strain rates as a result of their physical rock properties, emphasising the need to quantify the influence of these characteristics. Higher stresses result in lower apparent viscosities for multi-phase melt suspensions, and viscosity is strain rate dependent. Relative viscosity decreases as a function of strain, independent of crystal fraction under the range investigated, thus the previously termed "time-dependent" deformation should more properly be called "strain-dependent" deformation. With increasing strain, crystalline magmas follow a complex evolution of: elastic; strain hardening; constant-rate; and finally strain weakening behaviour in the approach to bulk failure. The strain at which these stages occur is dependent upon crystallinity, and other physical attributes (porosity and crystal size and shape distribution) which also significantly influence the mechanical characteristics. Strain-hardening results from the closure of pores, evidenced by porosity and permeability evolution, while the shear-thinning period is characterised by crystal rearrangement and magmatic flow and initiation of fractures in phenocrysts and groundmass. After a certain threshold (of strain, dependent upon stress) fracture coalescence and damage zone development begins to control the apparent viscosity, and behaviour deviates from that of magmatic flow. Although physical evidence shows that the samples experience significant damage, the axially-measured dynamic elastic moduli do not change significantly (due to the significant anisotropy developing in the deformed samples), and thus do not represent the true characteristics of the samples. We recommend that extreme care should be taken when using ultrasonic wave velocities as a proxy for strain (or damage).

Acknowledgements

The authors would like to thank O. Spieler and S. Mueller for sample collection and N. Varley for logistical organisation. D.B. Dingwell wishes to acknowledge the support of a research professorship of the Bundesexzellenzinitiative and an advanced grant (247076 EVOKES) of the European Research Council. Y. Lavallée wishes to acknowledge the support of the Deutsche Forschungsgemeinschaft grant LA2191/3-1 as well as the Starter Grant SLiM (306488) of the European Research Council. We acknowledge the support of a Hubert Curien Partnership (PHC) PROCOPE grant (grant number 27061UE) of the Deutscher Akademischer Austauschdienst (DAAD) in Germany, and the Ministry of Foreign and European Affairs (MAE) and the Ministry of Higher Education and Research (MESR), both in France. M. J. Heap also acknowledges CNRS INSU grant "Étude de la stabilité des édifices volcaniques".

Appendix A. Supplementary data

Supplementary data associated with this article can be found in the online version, at http://dx.doi.org/10.1016/j.jvolgeores.2013.05.012. These data include Google maps of the most important areas described in this article.

References

Arámbula-Mendoza, R., et al., 2011. Seismic activity that accompanied the effusive and explosive eruptions during the 2004–2005 period at Volcán de Colima, Mexico. Journal of Volcanology and Geothermal Research 205 (1–2), 30–46.

Atlas, Z.D., Dixon, J.E., Sen, G., Finny, M., Martin-Del Pozzo, A.L., 2006. Melt inclusions from Volcán Popocatépetl and Volcán de Colima, Mexico: melt evolution due to vapor-saturated crystallization during ascent. Journal of Volcanology and Geothermal Research 153 (3–4), 221–240.

Breton, M., Ramirez Ruiz, J.J., Navarro, C., 2002. Summary of the historical eruptive activity of Volcan de Colima, Mexico: 1519–2000. Journal of Volcanology and Geothermal Research 117, 21–46.

Caricchi, L., et al., 2007. Non-Newtonian rheology of crystal-bearing magmas and implications for magma ascent dynamics. Earth and Planetary Science Letters 264, 402–419.

Carreau, P.J., Lavoie, P.A., Yziquel, F., 1999. Rheological properties of concentrated suspensions. In: Siginer, D.D.K.D.A., Chhabra, R.P. (Eds.), Rheology Series. Elsevier, pp. 1299–1345.

Cimarelli, C., Costa, A., Mueller, S., Mader, H.M., 2011. Rheology of magmas with bimodal crystal size and shape distributions: insights from analog experiments. Geochemistry, Geophysics, Geosystems 12 (7), Q07024.

Cordonnier, B., Hess, K.-U., Lavallée, Y., Dingwell, D.B., 2009. Rheological properties of dome lavas: case study of Unzen volcano. Earth and Planetary Science Letters 279 (3–4), 263–272.

Costa, A., Sparks, R.S.J., Macedonio, G., Melnik, O., 2009. Effects of wall-rock elasticity on magma flow in dykes during explosive eruptions. Earth and Planetary Science Letters 288 (3–4), 455–462.

D'Oriano, C., et al., 2005. Changes in eruptive style during the A.D. 1538 Monte Nuovo eruption (Phlegrean Fields, Italy): the role of syn-eruptive crystallization. Bulletin of Volcanology 67 (7), 601–621.

Deubelbeiss, Y., Kaus, B.J.P., Connolly, J.A.D., Caricchi, L., 2011. Potential causes for the non-Newtonian rheology of crystal-bearing magmas. Geochemistry, Geophysics, Geosystems 12 (5), Q05007.

Dingwell, D.B., 1996. Volcanic dilemma: flow or blow? Science 273 (5278), 1054–1055.

Dingwell, D., Webb, S.L., 1989. Structural relaxation in silicate melts and non-Newtonian melt rheology in geologic processes. Physics and Chemistry of Minerals 16, 508–516.

Divoux, T., Vidal, V., Ripepe, M., Géminard, J.-C., 2011. Influence of non-Newtonian rheology on magma degassing. Geophysical Research Letters 38 (12), L12301.

Dominguez, T., Zobin, V.M., Reyes-Davila, G.A., 2001. The fracturing in volcanic edifice before an eruption: the June–July 1998 high-frequency earthquake swarm at Volcan de Colima, Mexico. Journal of Volcanology and Geothermal Research 105 (1–2), 65–75.

Edmonds, M., Herd, R.A., 2007. A volcanic degassing event at the explosive–effusive transition. Geophysical Research Letters 34 (21), L21310.

Gavilanes-Ruiz, J.C., et al., 2009. Exploring the factors that influence the perception of risk: the case of Volcán de Colima, Mexico. Journal of Volcanology and Geothermal Research 186 (3–4), 238–252.

Gent, A.N., 1960. Theory of the parallel plate viscometer. British Journal of Applied Physics 11 (2), 85.

Giordano, D., Russell, J.K., Dingwell, D.B., 2008. Viscosity of magmatic liquids: a model. Earth and Planetary Science Letters 271 (1–4), 123–134.
González, M.B., Ramírez, J.J., Navarro, C., 2002. Summary of the historical eruptive activity of Volcán De Colima, Mexico 1519–2000. Journal of Volcanology and Geothermal Research 117 (1–2), 21–46.
Guéguen, Y., Palciauskas, V., 1994. Introduction to the physics of rocks. Princeton University Press, Chichester, England.
Hawkins, A.B., 1998. Aspects of rock strength. Bulletin of Engineering Geology and the Environment 57, 17–30.
Heap, M.J., Vinciguerra, S., Meredith, P.G., 2009. The evolution of elastic moduli with increasing crack damage during cyclic stressing of a basalt from Mt. Etna volcano. Tectonophysics 471, 153–160.
Heap, M.J., Faulkner, D.R., Meredith, P.G., Vinciguerra, S., 2010. Elastic moduli evolution and accompanying stress changes with increasing crack damage: implications for stress changes around fault zones and volcanoes during deformation. Geophysical Journal International 183 (1), 225–236.
Heap, M.J., et al., 2011. Brittle creep in basalt and its application to time-dependent volcano deformation. Earth and Planetary Science Letters 307 (1–2), 71–82.
Hess, K.U., Cordonnier, B., Lavallée, Y., Dingwell, D.B., 2007. High-load, high-temperature deformation apparatus for synthetic and natural silicate melts. The Review of Scientific Instruments 78 (7), 075102.
Iverson, R.M., 2005. A dynamical model of seismogenic dome extrusion, Mount St. Helens, 2004–2005. Eos, Transactions of the American Geophysical Union V52B-04.
James, M.R., Varley, N., 2012. Identification of structural controls in an active lava dome with high resolution DEMs: Volcán de Colima, Mexico.
Kendrick, J.E., Smith, R., Sammonds, P., Meredith, P.G., Dainty, M., Pallister, J.S., 2013. The influence of thermal and cyclic stressing on the strength of rocks from Mount St. Helens, Washington. Bulletin of Volcanology 75 (7) (in press).
Kennedy, B., et al., 2005. Conduit implosion during Vulcanian eruptions. Geology 33 (7), 581–584.
Kolzenburg, S., et al., 2012. Strength and permeability recovery of tuffisite-bearing andesite. Solid Earth 3, 191–198.
Laumonier, M., Arbaret, L., Burgisser, A., Champallier, R., 2011. Porosity redistribution enhanced by strain localization in crystal-rich magmas. Geology 39 (8), 715–718.
Lavallée, Y., Hess, K.U., Cordonnier, B., Dingwell, D.B., 2007. Non-Newtonian rheological law for highly crystalline dome lavas. Geology 35 (9), 843–846.
Lavallée, Y., et al., 2008. Seismogenic lavas and explosive eruption forecasting. Nature 453 (7194), 507–510.
Lavallée, Y., et al., 2012. Magmatic architecture of dome-building eruptions at Volcán de Colima, Mexico. Bulletin of Volcanology 74 (1), 249–260.
Lejeune, A.M., Richet, P., 1995. Rheology of crystal-bearing silicate melts — an experimental study at high viscosities. Journal of Geophysical Research 100 (B3), 4215–4229.
Lensky, N.G., Sparks, R.S.J., Navon, O., Lyakhovsky, V., 2008. Cyclic activity at Soufrière Hills Volcano, Montserrat: degassing-induced pressurization and stick–slip extrusion. Geological Society, London, Special Publications 307 (1), 169–188.
Luhr, J.F., 2002. Petrology and geochemistry of the 1991 and 1998–1999 lava flows from Volcán de Colima, México: implications for the end of the current eruptive cycle. Journal of Volcanology and Geothermal Research 117 (1–2), 169–194.
Luhr, J.F., Carmichael, I.S.E., 1980. The Colima Volcanic Complex, Mexico: I. Post-caldera andesites from Volcan Colima. Contributions to Mineralogy and Petrology 71, 343–372.
Luhr, J.F., Carmichael, I.S.E., 1990. Petrological monitoring of cyclical eruptive activity at Volcán Colima, Mexico. Journal of Volcanology and Geothermal Research 42 (3), 235–260.
Manconi, A., et al., 2010. On the effects of 3-D mechanical heterogeneities at Campi Flegrei caldera, southern Italy. Journal of Geophysical Research—Solid Earth 115 (B8), B08405.
Marsh, B.D., 1981. On the crystallinity, probability of occurrence, and rheology of lava and magma. Contributions to Mineralogy and Petrology 78 (1), 85–98.
McBirney, A.R., Murase, T., 1984. Rheological properties of magmas. Annual Review of Earth and Planetary Sciences 12 (1), 337–357.
Melnik, O.E., 2001. An unsteady model for volcanic-eruption dynamics involving crystallization and through-magma gas filtration. Doklady Physics 46 (4), 271–275.
Melnik, O.E., Sparks, R.S.J., 1999. Nonlinear dynamics of lava dome extrusion. Nature 402, 37–41.
Melnik, O.E., Sparks, R.S.J., 2005. Controls on conduit magma flow dynamics during lava dome building eruptions. Journal of Geophysical Research 110 (B2), B02209.
Mora, J.C., et al., 2002. Petrology of the 1998–2000 products of Volcán de Colima, México. Journal of Volcanology and Geothermal Research 117 (1–2), 195–212.
Nakada, S., Shimizu, H., Ohta, K., 1999. Overview of the 1990–1995 eruption at Unzen Volcano. Journal of Volcanology and Geothermal Research 89, 1–22.
Navarro-Ochoa, C., Gavilanes-Ruíz, J.C., Cortés-Cortés, A., 2002. Movement and emplacement of lava flows at Volcán de Colima, México: November 1998–February 1999. Journal of Volcanology and Geothermal Research 117 (1–2), 155–167.
Pallister, J.S., Hoblitt, R.P., Crandell, D.R., Mullineaux, D.R., 1992. Mount St. Helens a decade after the 1980 eruptions: magmatic models, chemical cycles, and a revised hazards assessment. Bulletin of Volcanology 54 (2), 126–146.
Petford, N., 2003. Rheology of granitic magmas during ascent and emplacement. Annual Review of Earth and Planetary Sciences 31 (1), 399–427.
Picard, D., Arbaret, L., Pichavant, M., Champallier, R., Launeau, P., 2011. Rheology and microstructure of experimentally deformed plagioclase suspensions. Geology 39 (8), 747–750.
Reubi, O., Blundy, J., Varley, N., 2013. Volatiles contents, degassing and crystallisation of intermediate magmas at Volcán de Colima, Mexico, inferred from melt inclusions. Contributions to Mineralogy and Petrology 1–20.
Roscoe, R., 1952. The viscosity of suspensions of rigid spheres. British Journal of Applied Physics 3 (8), 267.
Savov, I.P., Luhr, J.F., Navarro-Ochoa, C., 2008. Petrology and geochemistry of lava and ash erupted from Volcán Colima, Mexico, during 1998–2005. Journal of Volcanology and Geothermal Research 174 (4), 241–256.
Smith, R., Sammonds, P.R., Kilburn, C.R.J., 2009. Fracturing of volcanic systems: experimental insights into pre-eruptive conditions. Earth and Planetary Science Letters 280 (1–4), 211–219.
Smith, R., Sammonds, P.R., Tuffen, H., Meredith, P.G., 2011. Evolution of the mechanics of the 2004–2008 Mt. St. Helens lava dome with time and temperature. Earth and Planetary Science Letters 307 (1–2), 191–200.
Sparks, R.S.J., 2003. Forecasting volcanic eruptions. Earth and Planetary Science Letters 210 (1–2), 1–15.
Sparks, R.S.J., Young, S.R., 2002. The eruption of Soufriere Hills Volcano, Montserrat (1995–1999): overview of scientific results. In: Druitt, T.H., Kokelaar, B.P. (Eds.), The Eruption of Soufriere Hills Volcano, Montserrat, from 1995 to 1999. Geological Society, London, pp. 45–69 (Memoirs).
Tuffen, H., Smith, R., Sammonds, P.R., 2008. Evidence for seismogenic fracture of silicic magma. Nature 453 (7194), 511–514.
Valdez-Moreno, G., Schaaf, P., Luis Macías, J., Kusakabe, M., 2006. New Sr–Nd–Pb–O isotope data for Colima volcano and evidence for the nature of the local basement. Geological Society of America Special Papers 402, 45–63.
Vallance, J.W., Schneider, D.J., Schilling, S.P., 2008. Growth of the 2004–2006 lava-dome complex at Mount St. Helens. In: Sherrod, D.R., Scott, W.E., Stauffer, P.H. (Eds.), A Volcano Rekindled: The Renewed Eruption of Mount St. Helens, 2004–2006: Professionnal Paper 1750. U.S. Geological Survey, pp. 169–208.
Varley, N., Arámbula-Mendoza, R., Reyes-Dávila, G., Sanderson, R., Stevenson, J., 2010. Generation of Vulcanian activity and long-period seismicity at Volcán de Colima, Mexico. Journal of Volcanology and Geothermal Research 198 (1–2), 45–56.
Webb, S.L., Dingwell, D.B., 1990. Non-Newtonian rheology of igneous melts at high stresses and strain rates: experimental results for rhyolite, andesite, basalt and nephelinite. Journal of Geophysical Research 95, 15695–15701.
Yong, C., Wang, C.Y., 1980. Thermally induced acoustic emission in rocks — influences of water and temperature disturbances. Geophysical Research Letters 7, 1089–1092.
Zobin, V.M., et al., 2002. Comparative characteristics of the 1997–1998 seismic swarms preceding the November 1998 eruption of Volcan de Colima, Mexico. Journal of Volcanology and Geothermal Research 117 (1–2), 47–60.
Zobin, V.M., et al., 2008. Monitoring the 2004 andesitic block-lava extrusion at Volcán de Colima, México from seismic activity and SO_2 emission. Journal of Volcanology and Geothermal Research 177 (2), 367–377.